

1 Microcarriers' suspension and flow dynamics in orbitally shaken
2 bioreactors

3 Pieralisi I.^a, Rodriguez G.^b, Micheletti M.^b, Paglianti A.^a, Ducci A.^c

4 ^aDipartimento di Ingegneria Civile, Chimica, Ambientale e dei Materiali, Universitá di Bologna, Via Terracini
5 28, 40131, Bologna, Italy

6 ^bUniversity College London, Department of Biochemical Engineering, WC1E 7JE, UK

7 ^cUniversity College London, Department of Mechanical Engineering, WC1E 7JE, UK

8 **Abstract**

In the present work an effort is made to determine the suspension speed of microcarriers in an orbitally shaken bioreactor of cylindrical geometry, and to assess the associated two-phase flow by means of Particle Image Velocimetry (PIV). Microcarrier technologies are commonly used in the bioprocess industry to culture adherent-dependent cells in three dimensional flow. Commercial GE Cytodex microcarriers were employed throughout this study to best mimic the flow conditions occurring in a bioreactor under standard operating conditions. Suspension speed measurements were obtained at different solid concentrations, that are typical for cell cultures, and for different combinations of orbital to cylinder diameters' ratio, d_o/d_i ($c = 2.5 - 12.5 \text{ g/L}$; $d_o/d_i = 0.2 - 0.7$; $N = 0 - 200 \text{ RPM}$). The current two-phase PIV results show that mean flow dynamics occurring in the cylindrical bioreactor are not significantly affected by the presence of the microcarriers, and that their suspension is directly associated to the flow transition reported by Weheliye et al. (2013). The flow scaling law included in their study can be successfully employed to predict the full suspension speed across bioreactors of different scales and working under different operating conditions (i.e. inner diameter of the cylinder, d_i , orbital diameter, d_o , and filling volume, V_f).

9 **Keywords:** Orbitally shaken bioreactor, microcarriers' suspension speed, PIV, two-phase flow.

10 **1. Introduction**

11 Stem cells represent attractive therapeutic agents for a wide range of diseases due to their ca-
12 pacity to differentiate into a specialized cell type. The large number of cells required for clinical
13 trials (up to millions cells/kg of body weight) demands a fast and reproducible expansion pro-
14 tocol. Stem cells are adherent-dependent cells, as they are able to grow and differentiate only
15 if attached to an appropriate support. Two-dimensional (2D) static culture methods rely on
16 the use of disposable multi-layer vessels and have rapidly become the most common route for
17 stem cells expansion (Simaria et al., 2014). However, these methods do not seem appropriate for
18 stem cell large scale production because of the limited cell productivity, labor intense handling
19 procedures and long cultivation times. For example, recent studies proved that commercial
20 requirements would be satisfied only with the production of up to 10^{13} cells per batch, and
21 the use of 10^5 layered vessels per lot, which is not a feasible process (Simaria et al., 2014). In

addition, these systems are not able to supply reproducible batch culture conditions (Mohamet et al., 2010). A cost-effective approach which has demonstrated to overcome many of the limitations of 2D cultures is represented by three-dimensional (3D) dynamic culture methods based on microcarriers suspension technologies (Frauenschuh et al., 2007; Sart et al., 2009; Storm et al., 2010). Microcarriers are generally spherical beads with an ideal size of 100-300 μm , and can be made of different materials (plastics, glass, silica dextran, collagen). Cell attachment is promoted through electrical charges or collagen coating. In microcarriers culture cells grow as monolayers on the surface of the beads or as multilayers in the pores of macroporous structures, that are usually suspended in culture medium by gentle stirring (GE Healthcare Life Sciences, 2013). With this technique the physiological microenvironment of stem cells can be easily monitored and reproduced, with significant advantages towards large scale production (King and Miller, 2007; Liu et al., 2014). The use of microcarriers in cell cultures allows an increase in the surface area (SA) per unit volume (cm^2/mL), improving product consistency and decreasing costs (Frauenschuh et al., 2007; Sart et al., 2009; Schop et al., 2008, 2009; Ferrari et al., 2012). Most studies have focused on investigating the optimal medium components, the microcarrier type and concentration, however only a few considered the engineering aspects, the quality of the microcarriers suspension and their impact on the liquid phase flow and turbulence levels. Conditions that promote efficient attachment and uniform distribution of the cells over the microcarriers population must be sought and optimized, and from this point of view, the flow and mixing dynamics occurring in the bioreactor must be thoroughly investigated and carefully selected. Efficient flow dynamics is crucial to achieve complete suspension of the microcarriers, thus preventing particle agglomeration and enhancing the available adherence area for the cells, while mixing is essential to promote mass transfer within the environment and to avoid spatial gradients in culture parameters (e.g. dissolved gases, nutrient concentration, pH), that can directly affect cell growth (Lara et al., 2006). At laboratory scale, adherent-dependent cell cultures are often grown on microcarriers in orbitally shaken reactors (OSRs), which offer an effective solution in the early stages of bioprocess development. Once the process is optimized, it is then scaled-up to traditional stirred tank reactors (STRs), where the velocity characteristics and turbulence levels are different from those found in shaken cultures. To overcome the scaling up/down limitations due to the different types of bioreactor, current bioprocess strategies have seen the development of miniature stirred tanks (for example the Ambr15 cell culture, 10-15 mL), to be employed in bioprocess development, while large scale shaken systems up to a scale of 1000 L have recently become available in the market, and studies have demonstrated their mixing effectiveness and oxygen transfer capabilities (Zhang et al., 2009).

Recently a few studies have focused on the mixing and fluid dynamics of shaken bioreactors. The works of Weheliye et al. (2013) and Ducci and Weheliye (2014) have provided a detailed understanding of the single-phase flow generated in an orbitally shaken bioreactor at different operating conditions (e.g. shaker rotational speed, N , and medium height inside the tank, h), geometrical characteristics (e.g. cylinder inner diameter, d_i , and orbital shaking diameter, d_o) and fluid viscosity, ν . A $Fr-Re$ flow transition map was derived, where four types of mean

63 flow were identified depending on the combination of Froude and Reynolds numbers selected.
 64 A transition from a toroidal to a precessional vortex configuration was detected with increasing
 65 Froude number, Fr , for fluids of water-like viscosity close to those employed in cell culture (high
 66 Re range). At low Fr the free surface exhibited an elliptic shape in phase with the shaker table
 67 orbital movement, while an increasing degree of out-of-phase and a highly three-dimensional free
 68 surface characterised the high end of shaker speeds investigated (Weheliye et al., 2013). A flow
 69 scaling law was derived to predict the occurrence of this flow transition based on the Froude
 70 number, Fr , the fluid non-dimensional height, h/d_i , and the orbital to cylinder diameter ratio,
 71 d_o/d_i . More specifically it was found that for $h/d_i \leq \sqrt{d_o/d_i}$ the critical Froude number can
 72 be obtained from Equation 1, and it is associated to the toroidal vortex reaching the bottom
 73 of the cylindrical bioreactor before transition occurs, while for $h/d_i \geq \sqrt{d_o/d_i}$ transition takes
 74 place without the toroidal vortex expanding all the way to the reactor bottom, and the critical
 75 speed/Froude number can be found from Equation 2.

$$Fr_{d_o} = \frac{1}{a_{ow}} \frac{h}{d_i} \left(\frac{d_o}{d_i} \right)^{0.5} \quad (1)$$

$$Fr_{d_i} = \frac{1}{a_{ow}} \quad (2)$$

76 Where a_{ow} is a constant depending on the fluid employed (1.4 for water), and the Froude number
 77 is defined as the ratio of the centrifugal to the gravitational accelerations, $Fr_d = 2\pi^2 N^2 d/g$,
 78 with d being either the orbital ($d = d_o$, Equation 1) or cylinder ($d = d_i$, Equation 2) diameters.
 79 The flow scaling law of Weheliye et al. (2013) was successfully applied to the mixing time exper-
 80 iments of Rodriguez et al. (2013, 2014) obtained by means of a base-acid colorisation technique
 81 in shaken bioreactors of cylindrical geometry. Rodriguez et al. (2014) compared their data to
 82 those obtained by Tissot et al. (2010) for very different operating conditions (d_o, V_f) and biore-
 83 actor sizes (d_i), and found out that the two sets of data scaled well when the mixing number
 84 was plotted against the ratio of Fr/Fr_{cr} , and achieved a constant value after flow transition
 85 occurred ($Fr > Fr_{cr}$).

86

87 Recently Mancilla et al. (2015) compared the mean flow and turbulence levels in orbitally shaken
 88 flasks with conventional, coiled, 1 and 3 baffle geometries. The 2D-PIV results obtained on a
 89 horizontal plane of measurements for increasing rotational speed, N , indicate that the config-
 90 uration with a single baffle is characterised by turbulence levels 25% higher than in the other
 91 configurations investigated, and should be employed for production of bacterial cultures. Nu-
 92 matical simulation studies of the flow dynamics in shaken systems have been carried out by
 93 Zhang et al. (2005) and Zhang et al. (2008) for 250-ml Erlenmeyer flasks and for 24-well and
 94 96-well bioreactors with water-like viscous fluids, respectively, while Kim and Kizito (2009) sim-
 95 ulated the flow in a cylindrical shaken bioreactor for different fluid viscosity. Discacciati et al.
 96 (2012) developed a pressure correction method to best capture the free surface deformation and
 97 assess the shear stress levels in an orbitally shaken cylindrical container for a high viscous fluid,
 98 while Reclari et al. (2014) compared the free surface wave measurements in a shaken cylinder
 99 against those predicted by a potential sloshing model, and identified the presence of different

100 modal responses inducing different flow regimes.

101

102 Little information can be found in the literature regarding the flow and mixing dynamics
103 taking place in bioreactors when microcarriers suspensions are considered. Collignon et al.
104 (2010) investigated the suspension of microcarriers for TTP Mixel, A325-A320 Lightnin, three
105 streambed-blades VMI-Rayneri, and Elephant Ear Applikon impellers in a stirred tank reactor,
106 and compared the flow characteristics, shear rate and power consumptions of the different im-
107 pellers at the corresponding just suspended speed, N_{js} . Their results indicated that the TTP
108 Mixel and the Ear Elephant Applikon impellers produced the lowest mechanical constraints at
109 their just suspended speed. PIV measurements in a spinner flask were carried out by Ismadi
110 et al. (2014) to assess to what extent flow shear stresses can affect cell culture of mouse induced
111 pluripotent stem cells (iPSC) attached to microcarriers. They show that optimum number of
112 cells was achieved over 7 days in 25 RPM suspension culture, corresponding to a maximum
113 shear of 0.0984 Pa. Nienow et al. (2014) developed a new method for the harvesting of human
114 mesenchymal stem cell (hMSC) in a spinner flask. The cells were cultured in dimple-bottomed
115 spinner flasks equipped with a magnetic horizontal stir bar and a vertical paddle at a working
116 volume of 100 mL and at 30 RPM (N_{JS}). After expansion, harvesting was implemented by
117 adding trypsin-EDTA and agitating the microcarriers suspension for 7 mins at 150 RPM. Their
118 study indicates that intense agitation for a short period (7 mins) under the presence of a suitable
119 enzyme can promote cell detachment without damaging the cells or affecting their attributes.
120 The overall harvesting efficiency was above 95 %.

121

122 Recently Olmos et al. (2015) determined the critical agitation speed for microcarriers' sus-
123 pension in orbitally shaken Erlenmeyer flasks and cylindrical reactors. They stained the micro-
124 carriers with Trypan blue and used a camera rigidly moving with the shaker table to assess their
125 suspension at increasing speed. The Vachy-Buckingham theorem was employed to obtain the
126 non-dimensional model of Equation 3.

$$\frac{N_s}{\sqrt{g/d_o}} = \sqrt{\frac{Fr_s}{2\pi^2}} = A \left(\frac{h}{d_i} \right)^{0.5} \left(\frac{d_o}{d_i} \right)^{0.25} (\rho^*) \left(\frac{d_p}{d_i} \right)^{-0.07} \quad (3)$$

127 Where A is a constant depending on the type of geometry used (1.39 for cylinder, 0.12 for
128 Erlenmeyer flask), and ρ^* and d_p are the relative density and diameter of the microcarriers,
129 respectively. It should be noted that in Equation 3 they considered a Froude number which is
130 defined as a velocity ratio, and it is related to the one defined in this work by the square root
131 of Fr . Direct comparison of Equations 1 and 3 shows that the critical Froude number, Fr_{cr} ,
132 associated to the flow transition reported by Weheliye et al. (2013), is related to the suspension
133 Froude number, Fr_s , obtained from the model of Olmos et al. (2015), with the non-dimensional
134 fluid height, h/d_i and orbital to cylinder diameter ratio, d_o/d_i , terms having the same exponents.
135 It is interesting to point out that their model showed a very good agreement also for Erlenmeyer
136 flasks, implying that a similar flow transition to the one reported by Weheliye et al. (2013) could
137 take place also in this geometry.

138

139 In the present study a different approach has been developed, where the “just-suspended” speed
140 is estimated from the light scattered by the microcarriers on a laser plane parallel to the bot-
141 tom of the cylindrical bioreactor, while vertical plane measurements were obtained to assess the
142 homogeneity of microcarriers across the tank volume. Furthermore, two-phase Particle Image
143 Velocimetry experiments were carried out to better comprehend the flow and mixing dynamics
144 in the presence of microcarriers, and to assess how their concentration affects the mean flow
145 characteristics.

146 **2. Materials and methods**

147 Depending on the measurements being carried out, two different experimental rigs were em-
148 ployed. Figure 1 (a) shows the experimental set-up used to obtain the “just suspended speed”,
149 where a 300 mW continuous diode laser, a mirror, a Net iCube camera with Macro Lens, and
150 a cylindrical bioreactor with a flat bottom, were all rigidly mounted on a Lab LS-X Kühner
151 shaker table. The laser-light was directed horizontally in order to illuminate the plane located
152 immediately over the vessel bottom, while a camera gained optical access to the measurement
153 plane through a mirror located underneath the bioreactor. The camera was equipped with a
154 macro lens with a shallow depth-of-field, that allowed to capture any small variation of the image
155 brightness, which was directly related to the light scattered by the microcarriers sitting at the
156 bottom of the bioreactor, as the shaking speed was varied. For each orbital speed investigated,
157 50 images were captured, and analysed by home-built Matlab routines to obtain a quantitative
158 average result of the suspension conditions of the system. Before capturing a set of images a
159 sufficient time was given to ensure steady-state condition was achieved at each speed investi-
160 gated. Experiments were carried out in a borosilicate glass cylindrical bioreactor of size $d_i = 7$
161 cm, for different ranges of orbital diameters, $d_o = 1.5 - 5$ cm, and shaker speeds, $N = 60 - 140$
162 RPM. The working liquid was distilled water with a fluid height $h = 3$ and 5 cm ($V_f = 115.5$,
163 192.5 mL). Commercial microcarriers, GE Cytodex 1 ($\rho = 1.03$ kg/L, $d_{50} = 190$ μm) and GE
164 Cytodex 3 ($\rho = 1.04$ kg/L, $d_{50} = 175$ μm), were employed at concentrations typically adopted
165 for stem cell cultures: 2.5, 7.5, 12.5 g/L (0.25, 0.75, 1.25 wt%). Their settling velocity was
166 approximately 0.6 mm/s. More information on the characteristics of the microcarriers employed
167 can be obtained in GE Healthcare Life Sciences (2013).

168

169 The two-phase PIV system is shown in Figure 1 (b), where a larger Kühner shaker table (1×1
170 m^2 , SR200-X shaker) is used to hold two cameras sharing the same field of view by a 50 %-
171 transmission/50 %-reflection mirror and an optical guiding arm shining the laser onto a mirror
172 positioned underneath the reactor. Contrary to the suspension speed experiments, in this case
173 the measurement region consisted on the vertical plane bisecting the bioreactor into two halves.
174 Each camera was equipped with a different light filter (either green, $\lambda = 532$ nm, or orange λ
175 = 570 nm) to distinguish between the solid and liquid phases. To improve the image quality of
176 the solid phase, fluorescent Rhodamine B isothiocyanate was employed to stain GE Cytodex 3

177 microcarriers, by exploiting the strong bond occurring between the dye and the thin collagen
 178 layer that coats the microcarriers' surface. The staining protocol consisted in mixing 2 mg of
 179 Rhodamine in 50 ml of deionized water for a 200 mg sample of GE Cytodex 3. Staining was done
 180 at room temperature for 12 hrs and a 45 μm sieve was used to filter the stained particles. After
 181 this procedure the two-phase measurements could be carried out up to a solid concentration of
 182 0.75 g/L (0.075 wt%). Above this threshold the image quality decreased due to the laser at-
 183 tenuation across the measurement plane induced by the presence of the microcarriers. Distilled
 184 water seeded with 1-40 μm flakes of painting was used as the continuous phase. Experiments
 185 were performed in a glass cylindrical bioreactor of size $d_i = 10$ cm, with an orbital diameter,
 186 $d_o = 5$ cm, and a fluid height $h = 5$ cm ($V_f = 392$ mL) for different shaker speeds, $N = 80 - 130$
 187 RPM.

188

189 Phase-locked measurements were obtained by a magnetic encoder coupled to the Kühner shaker
 190 table. The origin of the angular coordinate, ϕ , was set when the system reaches its position
 191 furthest to the left as the clockwise orbit is viewed from above. To fully resolve the large scale
 192 flow structures the measurement spatial resolutions of the liquid and solid phases were $\Delta x_i = 1.66$
 193 mm and 1.84 mm, respectively, while the time interval between PIV image pairs was $\Delta t = 1-2$ ms.
 194 The time interval, Δt , was selected according to the optimisation protocol developed by Gomez
 195 et al. (2010). In the rest of the article a cylindrical coordinate system r, ϕ, z is employed with the
 196 origin positioned on the cylinder axis at the bioreactor base. As mentioned in the introduction
 197 the Froude number based on the orbital diameter is an essential parameter to control the flow
 198 dynamics inside the bioreactor, and will be referred to here after either as Fr_{d_o} or, to simplify,
 199 as Fr . A comprehensive list of the operating conditions investigated for the suspension speed
 200 and PIV experiments is provided in Table 1.

201

| SUSPENDED SPEED | SOLID-LIQUID PIV |
|---|--|
| $d_i = 7$ cm | $d_i = 10$ cm |
| $d_o = 1.5, 2, 2.5, 3, 4, 5$ cm | $d_o = 5$ cm |
| $N = 0 - 200$ RPM | $N = 80, 90, 96, 110, 130$ RPM |
| $h = 2, 3, 4, 5$ cm ($V_f = 76.9 - 192.5$ mL) | $h = 5$ cm ($V_f = 392.5$ mL) |
| $c = 2.5, 7.5, 12.5$ g/L (0.25, 0.75, 1.25 wt%) | $c = 0.25, 0.5, 0.75$ g/L (0.025, 0.05, 0.075 wt%) |

Table 1: Geometrical details of the shaken systems and operational conditions investigated for the two-phase measurements.

202 **3. Results and discussion**

203 In the following sub-sections the three parts of the investigation, that is, microcarriers' suspen-
 204 sion speed (§ 3.1), microcarriers' dispersion (§ 3.2), and two-phase flow dynamics (§ 3.3), are

discussed in sequence. In brief, the rationale for the selection of these three parts of the work was to identify the range of speeds over which suspension occurs for different operating conditions, to assess the microcarriers' suspension and dispersion mechanisms as the shaker speed is increased, and to determine the flow dynamics and transition of the two-phase system as well as compare them against those obtained for a single-phase (Weheliye et al., 2013).

3.1. Microcarriers suspension speed

The just suspended speed was estimated from the brightness of the images taken on the horizontal measurement plane, which is directly proportional to the amount of particles sitting at the bottom of the reactor. The image brightness, $I_B(N)$, at a given shaking speed, N , is defined in Equation 4 by adding the pixel greyscale, p_{ij} , across the area delimited by the bioreactor walls on the horizontal plane of measurement:

$$I_B = \sum_{N_{tot}} p_{ij} \quad (4)$$

where N_{tot} is the total number of pixels across the area.

The microcarriers' suspension process and its correlation to the brightness percentage index, $I_B(N)/I_B(0)$, for increasing shaking speed, N , can be gained from Figure 2, where steady-state images of the microcarriers' concentration over horizontal planes are coupled to the $I_B(N)/I_B(0)$ curve at key speeds. This set of experiments was carried out for an orbital diameter $d_o = 2.5$ cm and a microcarriers' concentration $c = 2.5$ g/L. At low shaking speeds the microcarriers are uniformly distributed over the vessel bottom, and the brightness index is approximately constant up to a speed of 110 RPM, when the particles start being arranged in a spiral pattern on the bioreactor base and a drop of $I_B(N)/I_B(0)$ occurs. As the orbital speed is further increased a nearly constant value of the brightness index is attained above 150 RPM, implying that the "just-suspended" condition is achieved.

To better compare the results obtained for the different conditions analysed, the normalised brightness index, I^* , of Equation 5, which is scaled with the zero-speed, $I_B(0)$, and final-speed, $I_B(\infty)$, brightnesses, is used in the rest of the work.

$$I^* = \frac{I_B(N) - I_B(\infty)}{I_B(0) - I_B(\infty)} \quad (5)$$

The suspended speed is associated to a 95 % decrease of the brightness index with respect to the zero-speed condition, and it is identified as the speed at which $I^* = 5\%$. Based on the statistical error of the brightness index, $\approx 3\%$, and the non-linear regression method used to fit the data points, the uncertainty affecting the just suspended speed was found to be $\approx 5\%$. A video showing the particle suspension dynamics is also provided in the supplementary materials (**JS-Video.avi**). In this case however the shaker table was started from still conditions and, similarly to standard operating procedures, was gradually accelerated to a final speed of 140 rpm by the controller mounted on the shaker system (i.e. steady-state conditions were not achieved

at intermediate speeds). As a consequence the instantaneous velocity associated to each frame is unknown, and the following discussion is made in terms of number of revolutions of the shaker tray (i.e. the encoder was used to acquire a frame per revolution). In agreement with the data reported in Figure 2, darker zones start appearing at the periphery of the bioreactor ($t = 3 - 5$ s of the video), with microcarriers being more concentrated at the centre for increasing speed. This is well captured in Figure 3 (a), where the radial profiles of the normalised brightness index, $I^*(r)$, are shown for selected time instants, counted in number of revolutions, n , of the shaker tray, and corresponding to increasing shaking speed. After 100 revolutions, the shaker table has not gained a speed high enough to lift the particles, and the index I^* is nearly constant across the bioreactor diameter and close to unity. As the shaker table is accelerated a drop of I^* occurs after 110 revolutions, with the microcarriers being suspended for $r/R \geq 0.6$, while the center of the bioreactor, $r/R \leq 0.3$, is still unaffected after 130 revolutions. It is worth noticing that also the rate of suspension is lower in proximity of the bioreactor axis. For example, a 10 revolutions increment ($n = 120 - 130$) for $r/R \geq 0.6$ determines a variation of the normalised brightness index of $\Delta I^* \approx 0.45$, while a similar drop (≈ 0.5) occurs at $r/R = 0.3$ over a larger range of shaker revolutions, $\Delta n = 30$ ($n = 140 - 170$).

The spiral pattern, described in Figure 2 and shown in the supplementary video, is further analysed in Figure 3 (b), where the azimuthal profiles of I^* are plotted at $r/R = 0.8$ for an increasing number of shaker table revolutions ($n = 100 - 135$). It is evident that for $n = 110 - 122$ the profiles show a cyclic variation in the azimuthal direction, with 5 peaks over the range of θ considered. As expected the intensity of the profiles is decreasing as more microcarriers are lifted with increasing speed (i.e. number of revolutions), and the profiles are randomly shifted with respect to each other along θ , because the instants considered were taken far apart in time, and the spiral structure might have rotated with respect to the bioreactor. However an estimate of the spiral inclination can be gained from Figure 4 (a), where a single cycle of I^* has been obtained through a phase-average, $\langle \rangle$, along the azimuthal direction with a period $\Delta\theta = 20^\circ$. This analysis was performed at different radii for a single frame, $n = 117$. The phase-averaged profiles were normalised by their maximum variation $\langle \Delta I_B \rangle$, so that the final brightness parameter assumed a maximum absolute intensity of ≈ 1 for all the radii considered ($r/R = 0.6 - 0.9$). It should be noted that in Figure 4 (a) the flow direction is from right to left and opposite to that of θ . The peak shifts to the right as the radius increases, which means that the spiral is oriented towards the center in the direction of motion. The variation of the peak azimuthal coordinate, θ_{max} , against the radius is shown in Figure 4 (b) for two time instants, $n = 117$ and 120. The peak azimuthal coordinate, θ_{max} , shows a linear increase with r/R and the slope magnitude is nearly the same for both instants considered (i.e. 18.57° vs 18.86°). A visualisation of the spiral locus is provided in the inset diagram, where the arrow points in the flow direction.

The variation of I^* against the shaker tray speed is plotted in Figures 5 (a) and (b) for two orbital diameters, $d_o = 1.5$ and 2.5, respectively. Three different microcarriers' concentrations are considered, $c = 2.5, 7.5$ and 12.5 g/L, while the fluid height and vessel size are kept constant

($h = 5$ cm, $d_i = 7$ cm). It should be noted that by definition the index, I^* , can assume only values between 0 and 1 at high and low shaking speeds, respectively. Data points are fitted with the model of equation 6, where in the remainder part of the work the variable x can either be the shaker speed, N , or the Froude number ratio, Fr/Fr_{cr} .

$$I^*(x) = \frac{1}{1 + e^{a(x-x_0)}} \quad (6)$$

The parameters x_0 and a position the curve along the x coordinate, and control its rate of decay, respectively. The plots of Figure 5 (a) cross the 5 % reference line within a relative small range of suspension speeds, $N_s = 153 - 160$ RPM, and a correlation between the concentration and the suspension speed seems to be present (i.e. lower suspension speeds occur for lower concentrations). However this correlation is not present in the data of Figure 5 (b) for $d_o = 2.5$ cm, where an opposite behaviour is observed (i.e. lowest suspension speed for greatest concentration considered). Also in this case the range of variation of the suspended speed is relatively small, $N = 145 - 152$ RPM, and it is within the error of the measurement technique employed. Based on this consideration it was concluded that the concentration should not affect to a large extent the suspension of the microcarriers, at least within the range of concentration considered in this study, which includes those commonly employed in the bioprocess industry.

On the contrary the variation of the suspension speed with the orbital diameter is significant. This is evident in Figure 6 (a) where the normalised brightness index, I^* , is plotted against the shaker speed for different orbital diameter, $d_o = 1.5, 2.5$ and 5 cm. As expected the suspension speed, N_s , increases with decreasing orbital diameter, and assumes values of 120 RPM, 144 RPM and 153 RPM for $d_o = 5$ cm, 2.5 cm and 1.5 cm, respectively. In Figure 6 (b) an attempt was made to assess whether the suspension mechanism would scale with the critical Froude number ratio, Fr/Fr_{cr} . In fact the three systems are associated to different d_o/d_i and therefore reach the flow transition at different speeds (Weheliye et al., 2013). However the plot of Figure 6 (b) does not support this scaling procedure with the lowest (highest) orbital diameter still being associated to the greatest (lowest) critical Froude number ratio. This was explained by considering that the fluid height ($h = 5$ cm) of two, $d_o = 1.5$ cm and 2.5 cm, out of the three systems investigated is too large for the flow to fully develop to the cylinder bottom before transition occurs. In both cases $h/d_i > \sqrt{d_o/d_i}$ ($0.71 > 0.46$ for $d_o = 1.5$ cm and $0.71 > 0.59$ for $d_o = 2.5$ cm) and Equation 2 shall be used to determine the critical Froude number, Fr_{cr} .

Based on these considerations a second set of measurements was carried out to assess the suspension process when $h/d_i \leq \sqrt{d_o/d_i}$, and a critical speed exists for the flow to extend to the bottom of the reactor. The variation of I^* with d_o is provided in Figures 7 (a) and (b) for increasing speed and critical Froude number ratio, respectively. In agreement with Figure 6 (a) the plots of Figure 7 (a) intercept the 5% reference line at increasing suspension speed for decreasing orbital diameter. In this case however when the brightness index is plotted against the critical Froude number ratio (see Figure 7 b) the data tend to collapse on a single curve, indicating that the parameter Fr/Fr_{cr} can be successfully used for scaling across different configurations (i.e. d_o/d_i), provided that the fluid height satisfies the condition $h/d_i \leq \sqrt{d_o/d_i}$.

The data presented in Figures 6 and 7 are summarised in Figure 8, where the suspended to critical Froude number ratio is plotted against the parameter $h/d_i/\sqrt{d_o/d_i}$. As indicated by the inset schematics values of $h/d_i/\sqrt{d_o/d_i} < 1$ identify those configurations for which the toroidal vortices extend to the bottom of the bioreactor when the critical speed is achieved, while this does not occur for $h/d_i/\sqrt{d_o/d_i} > 1$, and flow transition takes place without the flow developing to the reactor base. The error bars in Figure 8 are supposed to provide a reference, and correspond to a 2 RPM variation in the suspension speed N_s (i.e. $dFr_s/Fr_{cr} = 2 \times (N_s/N_{cr}^2) dN_s$). From Figure 8, the 95 % suspension condition is achieved for $Fr_s/Fr_{cr} \leq 1.1$ when $h/d_i/\sqrt{d_o/d_i} < 1$, while the suspended to critical Froude number ratio tends to drift further away from the dashed reference line at $Fr_s/Fr_{cr} = 1.1$ as $h/d_i/\sqrt{d_o/d_i}$ increases above 1. It is interesting to note that the suspension speed data obtained by Olmos et al. (2015) in Erlenmeyer flasks showed a good scaling with the critical speed, N_{cr} , also for $h/d_i/\sqrt{d_o/d_i} > 1$.

333

The coefficients a and x_0 of Equation 6, used to determine the suspended to critical Froude number ratio (i.e. $Fr_s/Fr_{cr} = \log(19)/a + x_0$ for 95% suspension), are provided in Table 2. It is worth pointing that the range of variation of the decay coefficient for data associated to $h/d_i/\sqrt{d_o/d_i} > 1$ ($7 < a < 14.3$) is lower than that for $h/d_i/\sqrt{d_o/d_i} < 1$ ($14 < a < 17.8$). This implies that for $h/d_i/\sqrt{d_o/d_i} < 1$ suspension occurs more sharply with increasing speed.

| $h = 5 \text{ cm}$ | | | | | | $h = 3 \text{ cm}$ | | | | | |
|------------------------|----------------------------|---------|------------------------|---------|---------|----------------------|----------------------------|----------|-----------------------|-------|-------|
| $d_o = 1.5 \text{ cm}$ | | | $d_o = 2.5 \text{ cm}$ | | | $d_o = 5 \text{ cm}$ | | 2 cm | 3 cm | 4 cm | |
| | 2.5 g/L | 7.5 g/L | 12.5 g/L | 2.5 g/L | 7.5 g/L | 12.5 g/L | 7.5 g/L | 12.5 g/L | $c = 2.5 \text{ g/L}$ | | |
| a | 13.1 | 9.8 | 12.8 | 7.1 | 14.3 | 10 | 14 | 14.13 | 17.57 | 15.39 | 17.83 |
| x_0 | 1.05 | 1.05 | 1.19 | 0.87 | 0.98 | 0.87 | 0.72 | 0.74 | 0.95 | 0.92 | 0.94 |
| | $h/d_i/\sqrt{d_o/d_i} > 1$ | | | | | | $h/d_i/\sqrt{d_o/d_i} < 1$ | | | | |

Table 2: Coefficients a and x_0 obtained for all the sets of data analysed in this work.

338

3.2. Microcarriers' dispersion

A similar analysis to that employed in the previous section was carried out over vertical planes of measurement to assess the dispersion across the bioreactor of the microcarriers' suspension. In this case the normalisation of the brightness index was done according to Equation 7, where the coefficient varies from 0 (low concentration of microcarriers' over the volume) to 1 (homogenous concentration across the bioreactor volume).

$$I^* = \frac{I_B(N) - I_B(0)}{I_B(\infty) - I_B(0)} \quad (7)$$

The variation of I^* with the critical Froude number ratio, Fr/Fr_{cr} , is provided in Figure 9, where inset snapshots provide a visual reference of the degree of dispersion. Data refer to a

347 system with $d_i = 13$ cm, $d_o = 5$ cm and $h = 6.5$ cm ($h/d_i/\sqrt{d_o/d_i} < 1$). The vertical and horizon-
348 tal lines provide a reference of the suspended to critical Froude number ratio, $Fr_s/Fr_{cr} = 1.1$,
349 found in the previous section, and of the 95 % degree of homogeneity, respectively. From Figure
350 9 it can be concluded that complete dispersion is achieved at a speed slightly higher than the
351 suspended one, $\approx 1.2 \times Fr_{cr}$ (95 % threshold).

352

353 A closer view at the dispersion of microcarriers across the tank can be gained from the ax-
354 ial and radial cumulative brightness profiles of Figures 10 (a) and (b), respectively ($d_i = 10$ cm,
355 $d_o = h = 5$ cm). The axial (radial) cumulative brightness was obtained by adding the image
356 brightness along the radial (axial) direction. Before proceeding with the discussion, it is worth
357 mentioning that a limitation of adopting the brightness index as a reference for microcarriers'
358 concentration is that in the vertical plane of measurements the laser enters the bioreactor from
359 the base, and therefore complete brightness homogeneity is impossible to achieve due to reflec-
360 tions. This explains why brightness maxima are always located at $z = 0$, even at the higher speed
361 investigated, when microcarriers' suspension has certainly occurred. Despite this the current
362 data provide a reliable description of the suspension over a vertical plane for increasing speed.
363 Bearing this in mind, the plot of Figure 10 (a) shows that the axial distribution of microcarriers
364 is poor for $N \leq 100$ with the normalised brightness index, $I_B(z, N)/I_B(0, N)$, being relatively
365 low for $z/d_i \leq 0.04$, while, in agreement with the higher decay coefficients observed in Table 2
366 for $h/d_i/\sqrt{d_o/d_i} < 1$, a sharp change in $I_B(z, N)/I_B(0, N)$ occurs over a relatively small range of
367 shaker speeds, $N = 100 - 105$ RPM. The curves of $N = 105$ RPM and $N = 130$ RPM are nearly
368 parallel for $z/d_i \geq 0.06$ indicating that a similar degree of dispersion along the axial direction
369 has been achieved for both, while the lower intensity of $I_B(z, N)/I_B(0, N)$ indicates that fewer
370 microcarriers are suspended for the lower speed considered.

371

372 Similarly to the axial profiles, the radial profiles of the cumulative brightness index, $(I_B(z, N) -$
373 $I_B(0, N))/I_B(0, N)$, Figure 10 (b), show little suspension for $N < 102$, while at greater speeds
374 the radial distribution is characterised by double crested profiles, where the peaks capture the
375 higher microcarriers' concentration already present in the top-right inset of Figure 9. The peaks
376 are located close to the reactor axis and they occur in the region swept by the precessional vortex
377 once flow transition has occurred. Based on these results and those in the previous section it
378 can be concluded that microcarriers are pushed from the periphery towards the centre of the
379 reactor base, and they are then sucked into the bulk flow by the depression created close to the
380 axis of the bioreactor by the two-counter rotating and precessional vortices, before and after
381 flow transition, respectively.

382 *3.3. Two-phase flow dynamics*

383 Two-phase Particle Image Velocimetry experiments were carried out to better understand the
384 influence of the solid phase on the mean characteristics of the flow, and to assess whether the
385 flow transition reported by Weheliye et al. (2013) can be extended to the two-phase system. A
386 preliminary analysis was carried out to assess whether the free surface wave, which is the flow

driving mechanism, is affected by the microcarriers' concentration. The study of Weheliye et al. (2013) showed that for a single-phase system the nondimensional wave amplitude, $\Delta h/d_i$, is proportional to the Froude number, meaning that for selected combinations of N and d_o , the free surface will assume a fixed inclination, which is independent of the fluid height h and vessel diameter, d_i . The constant of proportionality, a_o , depends on the fluid considered, and is equal to 1.4 in the case of water, and decreases with increasing fluid viscosity (Ducci and Weheliye, 2014). The variation of $\Delta h/d_i$ against Fr ($0.25 < Fr < 0.5$) for different microcarriers' concentrations at $h/d_i = 0.5$, and $d_o/d_i = 0.5$ is provided in Figure 11. The data points are all located close to the reference line, which corresponds to a single-phase system with water as the working fluid ($a_{ow} = 1.4$). A small decrease of the slope might be seen for increasing microcarriers' concentrations, that is consistent with the behaviour reported by Ducci and Weheliye (2014) for increasing viscosity. This means that the flow dynamics of the two-phase system is not remarkably affected by the presence of microcarriers at the concentration considered, and that the applicability of the relation found by Weheliye et al. (2013) can be extended to the two-phase system. Lower values of the slope coefficient, a_o , might imply that the critical Froude number for the two-phase system is slightly higher than that of the single-phase (see Equation 1), and therefore the suspended speed data points of Figure 8 might get closer to the horizontal reference line of $Fr/Fr_{cr} = 1$.

The phase-resolved velocity vector fields and tangential vorticity, $\omega_\theta/(\pi N)$, contour maps of the liquid and solid phases are shown in Figure 12 (a-b) and (c-d) for in-phase, prior to flow transition, and out-of-phase conditions, respectively. For both flow conditions the phase angle was $\phi = 0$ and the microcarriers' concentration, $c = 0.5 \text{ g/L}$. The velocity fields of the liquid and solid phases for in-phase flow (Figures 12 a and b) are qualitatively similar to each other, and are characterised by the two vortical cell configuration already identified by Weheliye et al. (2013) at the same speed for single-phase flow. However, in the toroidal vortex region, the vorticity of the solid phase assumes values slightly higher than for the liquid one (mainly on the left hand side vortex), indicating that a slip velocity is present between the two phases. Similar conclusions can be drawn when comparing the velocity fields for the out of phase flow (Figures 12 c and d). In this case the axial slip velocity, $|u_{z_S} - u_{z_L}| < 0.02 \times \pi N d_o$ (0.6 mm/s). It is worth mentioning that this range of values is comparable to the average and maximum velocities of the liquid phase over the plane of measurement, 0.033 and $0.10 \times \pi N d_o$, respectively.

4. Conclusions

This study is the first one to provide insight on the two-phase flow dynamics occurring in an orbitally shaken bioreactor when microcarriers are used in suspension under real process conditions. The suspension dynamics of the two-phase system was investigated using a visualization approach, which allowed to estimate the "just - suspended" shaking speed from the light scattered by the microcarriers on a laser plane parallel to the bottom of the cylindrical bioreactor. The shaking system was studied varying solid concentration and orbital diameter, and the results highlighted the correlation between the microcarriers suspension and the critical Froude

number corresponding to the occurrence of the flow transition identified by Weheliye et al. (2013) for a single-phase system. It was found that for bioreactor configurations corresponding to $h/d_i/\sqrt{d_o/d_i} < 1$ the suspended Froude number, Fr_s , is nearly constant and equal to $1.1 \times Fr_{cr}$, while for $h/d_i/\sqrt{d_o/d_i} > 1$ the suspended speed tends to increase, and suspension is delayed to higher speeds after flow transition. From this point of view the first type of configuration should be sought because it achieves full suspension and at the same time minimises power consumption and shear rates.

434

An analysis of the suspension mechanisms highlighted that microcarriers are pushed from the periphery towards the centre of the reactor base along a spiral pattern, and then they are sucked into the bulk flow by the depression created close to the axis of the bioreactor by the two-counter rotating and precessional vortices, before and after flow transition, respectively. Vertical plane measurements were used to assess the homogeneity of the microcarriers across the reactor volume, and it was found that full dispersion is achieved at $\approx 1.2 \times Fr_{cr}$. A model was developed to fit the suspension data, and showed that suspension dynamics are faster and occur over a narrower range of speeds for $h/d_i/\sqrt{d_o/d_i} < 1$. The free surface experiments validated the relation found by Weheliye et al. (2013) between the non-dimensional wave amplitude of the cylindrical bioreactor, $\Delta h/d_i$, and the Froude number, and it was found that the presence of the microcarriers might reduce the constant of proportionality between the two parameters, and result in slightly higher critical Froude number, Fr_{cr} . The velocity fields of the liquid and solid phases were simultaneously measured over a vertical plane bisecting the vessel, and their mean flows were found to be very similar both for in-phase and out-of-phase conditions. This is in agreement with previous studies on stirred tank reactors where low solid concentrations are employed. The range of variation of the axial slip velocity, $|u_{zS} - u_{zL}| < 0.02 \times \pi N d_o$ (0.6 mm/s), was comparable in magnitude to the average and maximum velocities of the liquid phase over the plane of measurement, 0.033 and $0.10 \times \pi N d_o$, respectively.

453

Further studies are called for to investigate the suspension dynamics of the next generation of microcarriers. Biodegradable materials are increasingly used to make microcarriers for cell adherent applications in order to avoid the need for the cell detachment and recovery steps. However the materials used are often characterised by densities much heavier than water, thus requiring considerable energy to be suspended. The flow visualisation methodology established in this work, as well as the simultaneous measurement of the two-phase flow characteristics, could be implemented for other microcarriers' types to assess the quality of suspension, and its dependence on the bioreactor geometry and operating conditions.

462 **Nomenclature**

463 **Abbreviation**

| | | |
|-----|-----|-----------------------------|
| 464 | 2D | Two-Dimensional |
| 465 | OSB | Orbitally shaken bioreactor |
| 466 | STR | Stirred Tank Reactor |
| 467 | PIV | Particle Image Velocimetry |
| 468 | 3D | Three-Dimensional |

469

470 **Greek Symbols**

| | | |
|-----|------------|--|
| 471 | ν | Kinematic viscosity, m ² /s |
| 472 | ρ | Microcarriers' density kg/m ³ |
| 473 | ρ^* | Microcarriers' relative density, - |
| 474 | ϕ | Phase angle of the table, ° |
| 475 | ω_i | Vorticity component in the i th direction, s ⁻¹ |

476

477 **Roman Symbols**

| | | |
|-----|---------------|---|
| 478 | a | Decay coefficient of Equation 6, - |
| 479 | a_{ow} | Constant of proportionality for water, - |
| 480 | d_i | Inner diameter of the cylinder, m |
| 481 | d_o | Orbital diameter, m |
| 482 | d_p, d_{50} | Microcarriers' diameter, m |
| 483 | Fr | Froude number, - |
| 484 | Fr_{cr} | Critical/transitional Froude number, - |
| 485 | Fr_s | Suspended Froude number, - |
| 486 | g | Gravitational acceleration, m/s ² |
| 487 | h | Fluid height at rest, m |
| 488 | Δh | Free surface height, m |
| 489 | I^* | Normalised brightness index, - |
| 490 | I_B | Brightness index, - |
| 491 | n | Number of shaker revolution, - |
| 492 | N | Shaking frequency, s ⁻¹ |
| 493 | N_{cr} | Critical shaking frequency, s ⁻¹ |
| 494 | N_s | Suspension shaking frequency, s ⁻¹ |
| 495 | R | Inner radius of the cylinder, m |
| 496 | Re | Reynolds number, - |
| 497 | u_i | Velocity in the i th direction, m/s |
| 498 | V_f | Fluid filling volume, m ³ |
| 499 | x_0 | Position coefficient of Equation 6, - |

500 **List of Figures**

| | | |
|-----------|--|----|
| 501 1 | Experimental set-ups: (a) suspended speed; (b) two-phase PIV. | 19 |
| 502 2 | Visualization of the suspension mechanism and variation of the brightness percentage index, $I_B(N)/I_B(0)$, with shaking speed ($d_o = 1.5$ cm, $h = 5$ cm, $c = 2.5$ g/L). | 20 |
| 503 3 | Profiles of the normalised brightness index I^* for increasing number of shaker revolutions ($d_o = 2$ cm, $h = 3$ cm, $c = 2.5$ g/L): (a) radial profiles; (b) azimuthal profiles ($r/R = 0.8$). | 21 |
| 504 4 | (a) Phase-averaged azimuthal profiles of the image brightness at $n = 117$ for different radii ($r/R = 0.6 - 0.9$); (b) Radial and azimuthal coordinates of the brightness peak for $n = 117$ and 120 ($d_o = 2$ cm, $h = 3$ cm, $c = 2.5$ g/L). | 22 |
| 505 5 | Variation of I^* with shaker speed for different microcarriers' concentrations ($h = 5$ cm, $d_i = 7$ cm): (a) $d_o = 1.5$ cm; (b) $d_o = 2.5$ cm. | 23 |
| 506 6 | Variation of I^* for different orbital diameters ($h = 5$ cm, $d_i = 7$ cm, $c = 2.5$ g/L): (a) variation with shaker speed, N ; (b) variation with Fr/Fr_{cr} | 24 |
| 507 7 | Variation of I^* for different orbital diameters ($h = 3$ and 5 cm, $d_i = 7$ cm, $c = 2.5$ g/L): (a) variation with shaker speed, N ; (b) variation with Fr/Fr_{cr} | 25 |
| 508 8 | Variation of the suspended to critical Froude number ratio, Fr_s/Fr_{cr} , with critical height ratio, $\frac{h}{d_i}/\sqrt{\frac{d_o}{d_i}}$, for all the conditions investigated. | 26 |
| 509 9 | Variation of the normalised brightness index, I^* , with the Froude number ratio, Fr/Fr_{cr} , obtained from measurements on a vertical plane ($d_i = 13$ cm, $d_o = 5$ cm, $h = 6.5$ cm). | 27 |
| 510 10 | Profiles of the axial and radial cumulative brightness indices for increasing shaken speed ($d_i = 10$ cm, $d_o = 5$ cm, $h = 5$ cm): (a) Axial profiles; (b) Radial profiles. . | 28 |
| 511 11 | (a) Variation of the non-dimensional wave amplitude, $\Delta h/d_i$, with Froude number, Fr , for different microcarriers' concentrations ($h = 5$ cm, $d_i = 10$ cm, $d_o = 5$ cm). | 29 |
| 512 12 | (a) Velocity vector fields and tangential vorticity contour maps of the liquid and solid phases before and after flow transition ($h = 5$ cm, $d_i = 10$ cm, $d_o = 5$ cm, $c = 0.5$ g/L): (a) Liquid phase, $N = 90$ RPM; (b) Solid phase, $N = 90$ RPM; (c) Liquid phase, $N = 110$ RPM; (d) Solid phase, $N = 110$ RPM | 29 |

531 **References**

- 532 Collignon, M.L.L., Delafosse, A., Crine, M., Toye, D., 2010. Axial impeller selection for anchor-
533 age dependent animal cell culture in stirred bioreactors: Methodology based on the impeller
534 comparison at just-suspended speed of rotation. *Chemical Engineering Science* 65, 5929–5941.
- 535 Discacciati, M., Hacker, D., Quarteroni, A., Quinodoz, S., Tissot, S., Wurm, F.M., 2012. Nu-
536 matical simulation of orbitally shaken viscous fluids with free surface. *International Journal*
537 for Numerical Methods in Fluids , 1–14.
- 538 Ducci, A., Weheliye, W.H., 2014. Orbitally shaken bioreactors - Viscosity effects on flow char-
539 acteristics. *AIChE Journal* 60, 3951–3968.
- 540 Ferrari, C., Balandras, F., Guedon, E., Olmos, E., Chevalot, I., Marc, A., 2012. Limiting cell
541 aggregation during mesenchymal stem cell expansion on microcarriers. *Biotechnology Progress*
542 28, 780–787.
- 543 Frauenschuh, S., Reichmann, E., Ibold, Y., Goetz, P.M., Sittinger, M., Ringe, J., 2007. A
544 microcarrier-based cultivation system for expansion of primary mesenchymal stem cells.
545 *Biotechnology Progress* 23, 187–193.
- 546 GE Healthcare Life Sciences, 2013. Microcarrier Cell Culture-Principles & Methods. Technical
547 Report.
- 548 Gomez, C., Bennington, C.P.J., Taghipour, F., 2010. Investigation of the Flow Field in a
549 Rectangular Vessel Equipped With a Side-Entering Agitator. *Journal of Fluids Engineering*
550 132, 051106.
- 551 Ismadi, M.Z., Gupta, P., Fouras, A., Verma, P., Jadhav, S., Bellare, J., Hourigan, K., 2014.
552 Flow characterization of a spinner flask for induced pluripotent stem cell culture application.
553 *PloS one* 9, e106493.
- 554 Kim, H.M., Kizito, J.P., 2009. Stirring Free Surface Flows Due To Horizontal Circulatory
555 Oscillation of a Partially Filled Container. *Chemical Engineering Communications* 196, 1300–
556 1321.
- 557 King, J.A., Miller, W.M., 2007. Bioreactor development for stem cell expansion and controlled
558 differentiation. *Current Opinion in Chemical Biology* 11, 394–398.
- 559 Lara, A.R., Galindo, E., Ramírez, O.T., Palomares, L.A., 2006. Living with heterogeneities in
560 bioreactors: understanding the effects of environmental gradients on cells. *Molecular biotech-*
561 *nology* 34, 355–381.
- 562 Liu, N., Zang, R., Yang, S.T., Li, Y., 2014. Stem cell engineering in bioreactors for large-scale
563 bioprocessing. *Engineering in Life Sciences* 14, 4–15.

- 564 Mancilla, E., Palacios-Morales, C.A., Córdova-Aguilar, M.S., Trujillo-Roldán, M.A., Ascanio,
565 G., Zenit, R., 2015. A hydrodynamic description of the flow behavior in shaken flasks. Bio-
566 chemical Engineering Journal 99, 61–66.
- 567 Mohamet, L., Lea, M.L., Ward, C.M., 2010. Abrogation of E-cadherin-mediated cellular aggre-
568 gation allows proliferation of pluripotent mouse embryonic stem cells in shake flask bioreactors.
569 PloS one 5, e12921.
- 570 Nienow, A.W., Rafiq, Q.A., Coopman, K., Hewitt, C.J., 2014. A potentially scalable method
571 for the harvesting of hMSCs from microcarriers. Biochemical Engineering Journal 85, 79–88.
- 572 Olmos, E., Loubiere, K., Martin, C., Delaplace, G., Marc, A., 2015. Critical agitation for
573 microcarrier suspension in orbital shaken bioreactors: Experimental study and dimensional
574 analysis. Chemical Engineering Science 122, 545–554.
- 575 Reclari, M., Dreyer, M., Tissot, S., Obreschkow, D., Wurm, F.M., Farhat, M., 2014. Surface
576 wave dynamics in orbital shaken cylindrical containers. Physics of Fluids 26.
- 577 Rodriguez, G., Anderlei, T., Micheletti, M., Yianneskis, M., Ducci, A., 2014. On the measure-
578 ment and scaling of mixing time in orbitally shaken bioreactors. Biochemical Engineering
579 Journal 82, 10–21.
- 580 Rodriguez, G., Weheliye, W., Anderlei, T., Micheletti, M., Yianneskis, M., Ducci, A., 2013. Mixing
581 time and kinetic energy measurements in a shaken cylindrical bioreactor. Chemical
582 Engineering Research and Design 91, 2084–2097.
- 583 Sart, S., Schneider, Y.J., Agathos, S.N., 2009. Ear mesenchymal stem cells: an efficient adult
584 multipotent cell population fit for rapid and scalable expansion. Journal of biotechnology 139,
585 291–299.
- 586 Schop, D., Janssen, F.W., Borgart, E., de Bruijn, J.D., van Dijkhuizen-Radersma, R., 2008. Expansion
587 of mesenchymal stem cells using a microcarrier-based cultivation system: growth
588 and metabolism. Journal of tissue engineering and regenerative medicine 2, 126–135.
- 589 Schop, D., Janssen, F.W., van Rijn, L.D.S., Fernandes, H., Bloem, R.M., de Bruijn, J.D., van
590 Dijkhuizen-Radersma, R., 2009. Growth, metabolism, and growth inhibitors of mesenchymal
591 stem cells. *Tissue Engineering - Part A* 15.
- 592 Simaria, A.S., Hassan, S., Varadaraju, H., Rowley, J., Warren, K., Vanek, P., Farid, S.S.,
593 2014. Allogeneic cell therapy bioprocess economics and optimization: single-use cell expansion
594 technologies. Biotechnology and bioengineering 111, 69–83.
- 595 Storm, M.P., Orchard, C.B., Bone, H.K., Chaudhuri, J.B., Welham, M.J., 2010. Three-
596 dimensional culture systems for the expansion of pluripotent embryonic stem cells. Biotech-
597 nology and bioengineering 107, 683–695.

- 598 Tissot, S., Farhat, M., Hacker, D.L., Anderlei, T., Kühner, M., Comninellis, C., Wurm, F., 2010.
599 Determination of a scale-up factor from mixing time studies in orbitally shaken bioreactors.
600 Biochem. Eng. J. 52, 181–186.
- 601 Weheliye, W., Yianniskis, M., Ducci, A., 2013. On the Fluid Dynamics of Shaken Bioreactors
602 - Flow Characterization and Transition. AIChE Journal 59, 334–344.
- 603 Zhang, H., Lamping, S.R., Pickering, S.C.R., Lye, G.J., Shamlou, P.A., 2008. Engineering
604 characterisation of a single well from 24-well and 96-well microtitre plates. Biochem. Eng. J.
605 40, 138–149.
- 606 Zhang, H., Williams-Dalson, W., Keshavarz-Moore, E., Shamlou, P.A., 2005. Computational-
607 fluid-dynamics (CFD) analysis of mixing and gas-liquid mass transfer in shake flasks. Biotech-
608 nology and applied biochemistry 41, 1–8.
- 609 Zhang, X., Bürki, C.A.A., Stettler, M., De Sanctis, D., Perrone, M., Discacciati, M., Parolini,
610 N., DeJesus, M., Hacker, D.L., Quarteroni, A., Wurm, F.M., 2009. Efficient oxygen transfer by
611 surface aeration in shaken cylindrical containers for mammalian cell cultivation at volumetric
612 scales up to 1000L. Biochem. Eng. J. 45, 41–47.

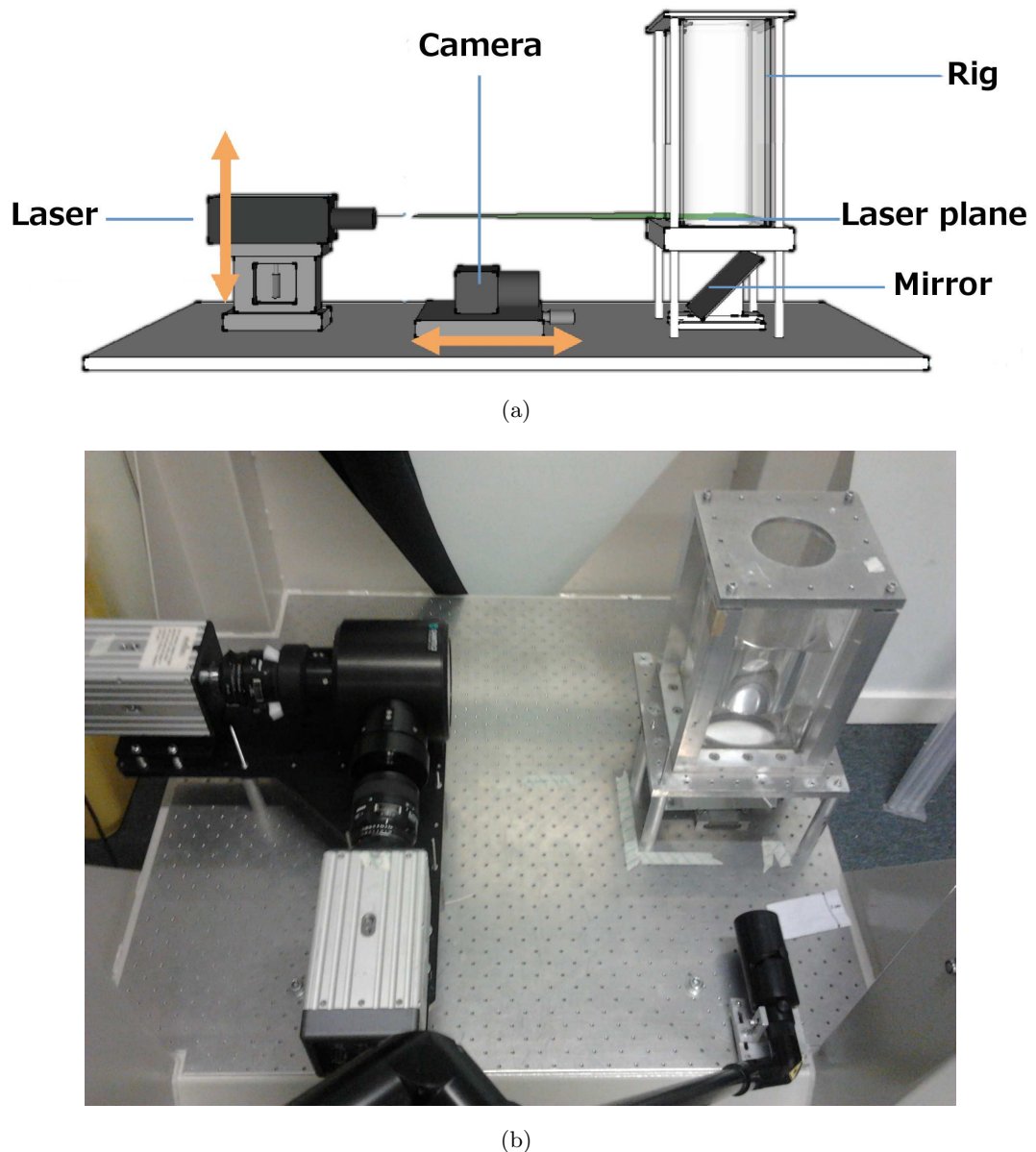


Figure 1: Experimental set-ups: (a) suspended speed; (b) two-phase PIV.

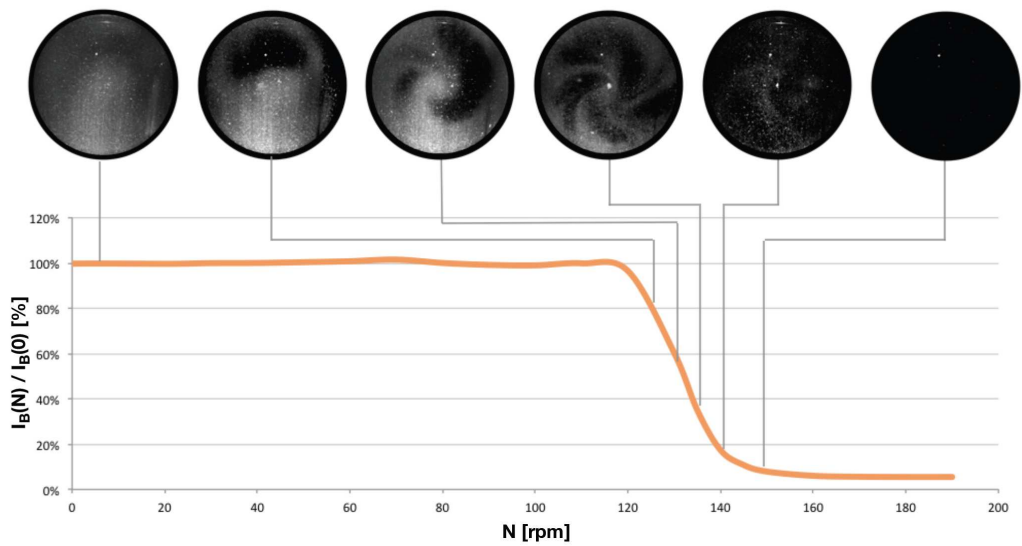


Figure 2: Visualization of the suspension mechanism and variation of the brightness percentage index, $I_B(N)/I_B(0)$, with shaking speed ($d_o = 1.5$ cm, $h = 5$ cm, $c = 2.5$ g/L).

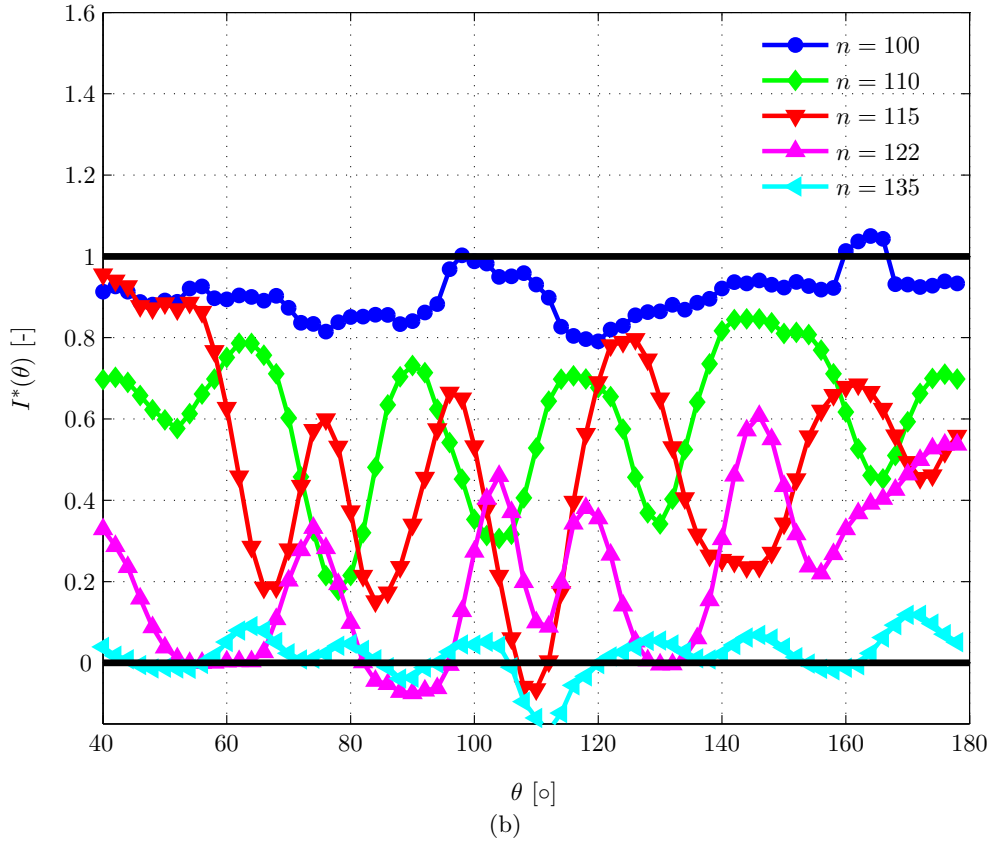
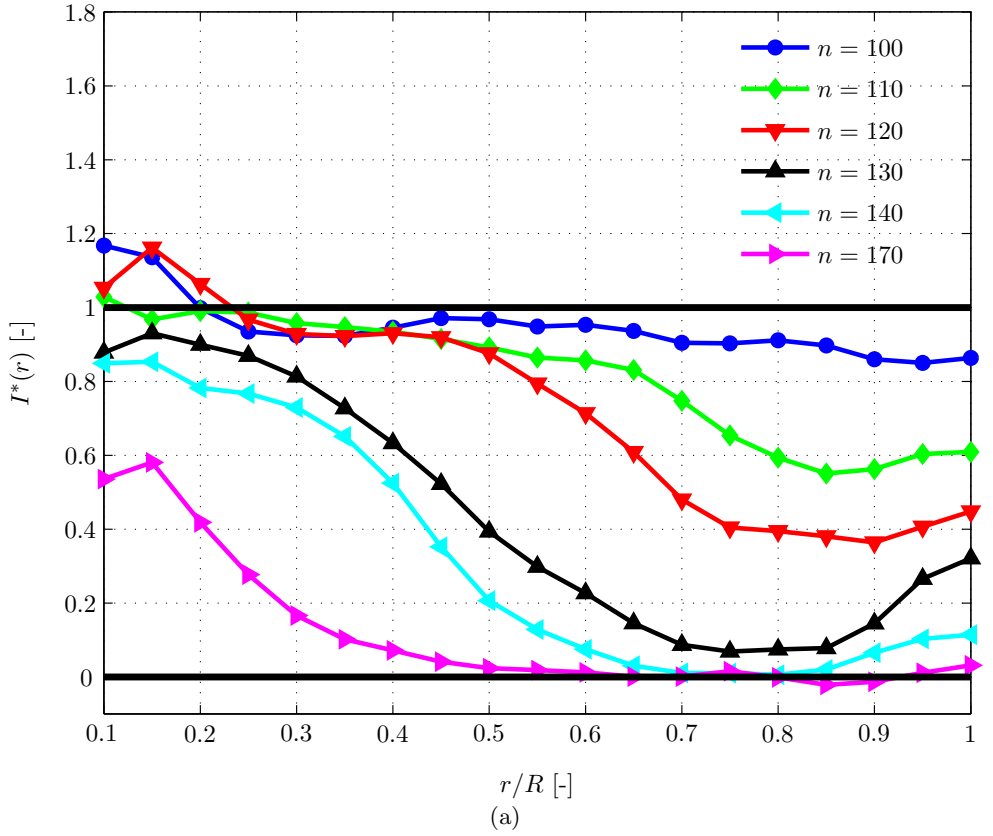
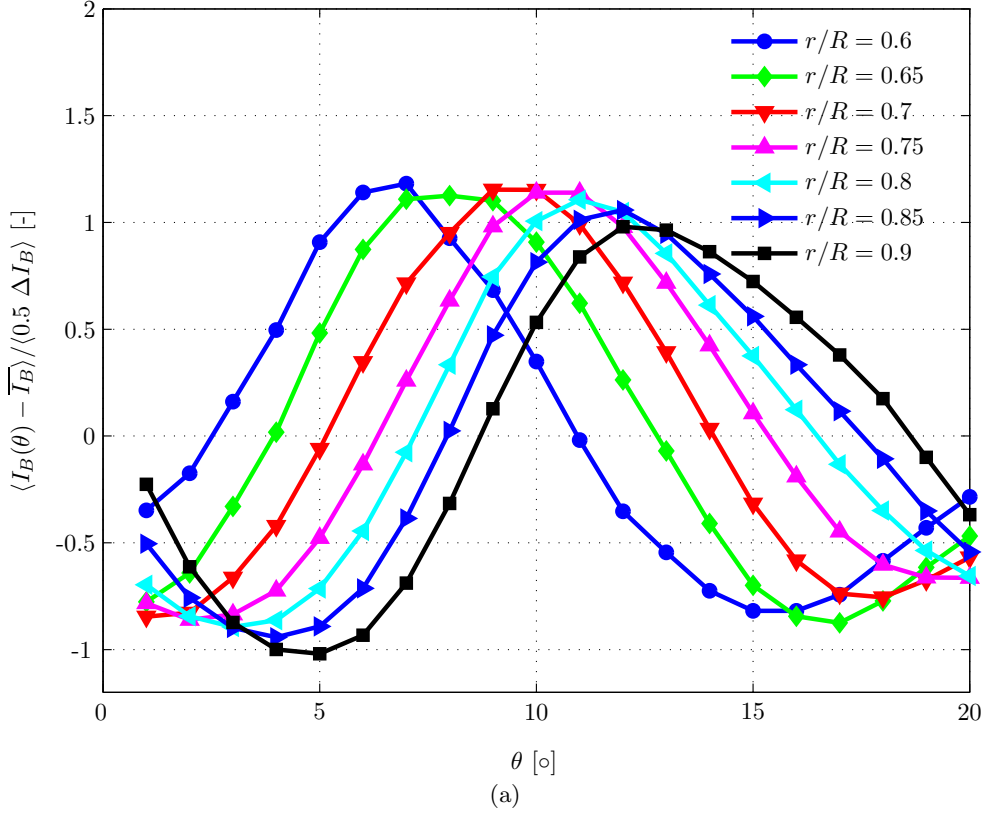
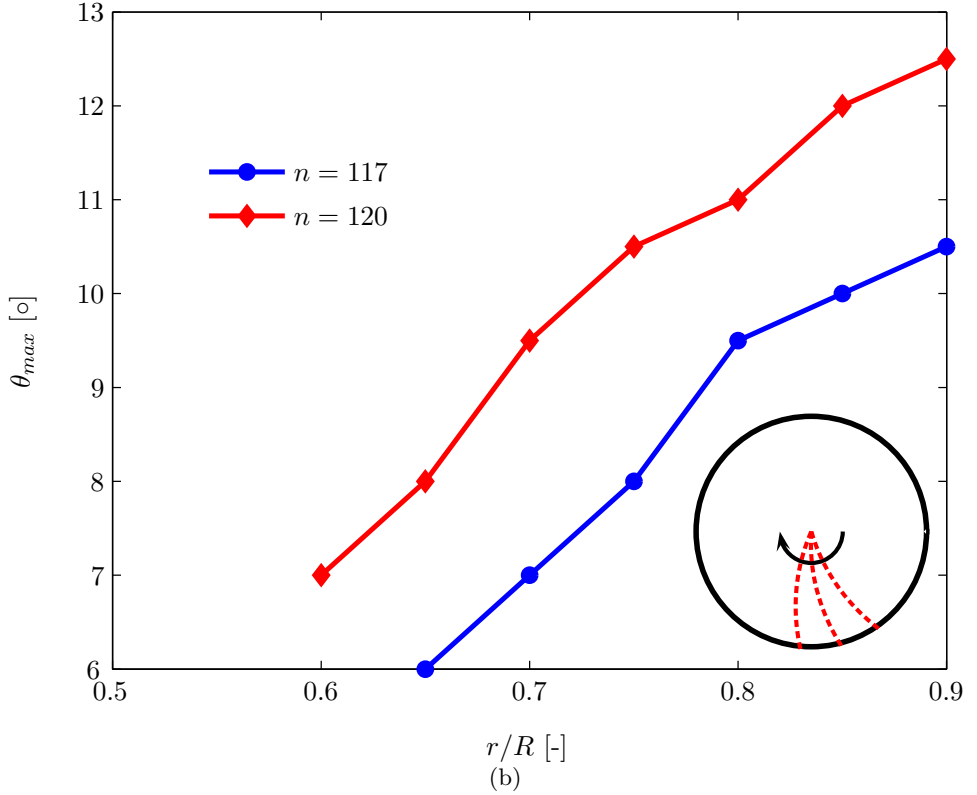


Figure 3: Profiles of the normalised brightness index I^* for increasing number of shaker revolutions ($d_o = 2$ cm, $h = 3$ cm, $c = 2.5$ g/L): (a) radial profiles; (b) azimuthal profiles ($r/R = 0.8$).



(a)



(b)

Figure 4: (a) Phase-averaged azimuthal profiles of the image brightness at $n = 117$ for different radii ($r/R = 0.6 – 0.9$); (b) Radial and azimuthal coordinates of the brightness peak for $n = 117$ and 120 ($d_o = 2$ cm, $h = 3$ cm, $c = 2.5$ g/L).

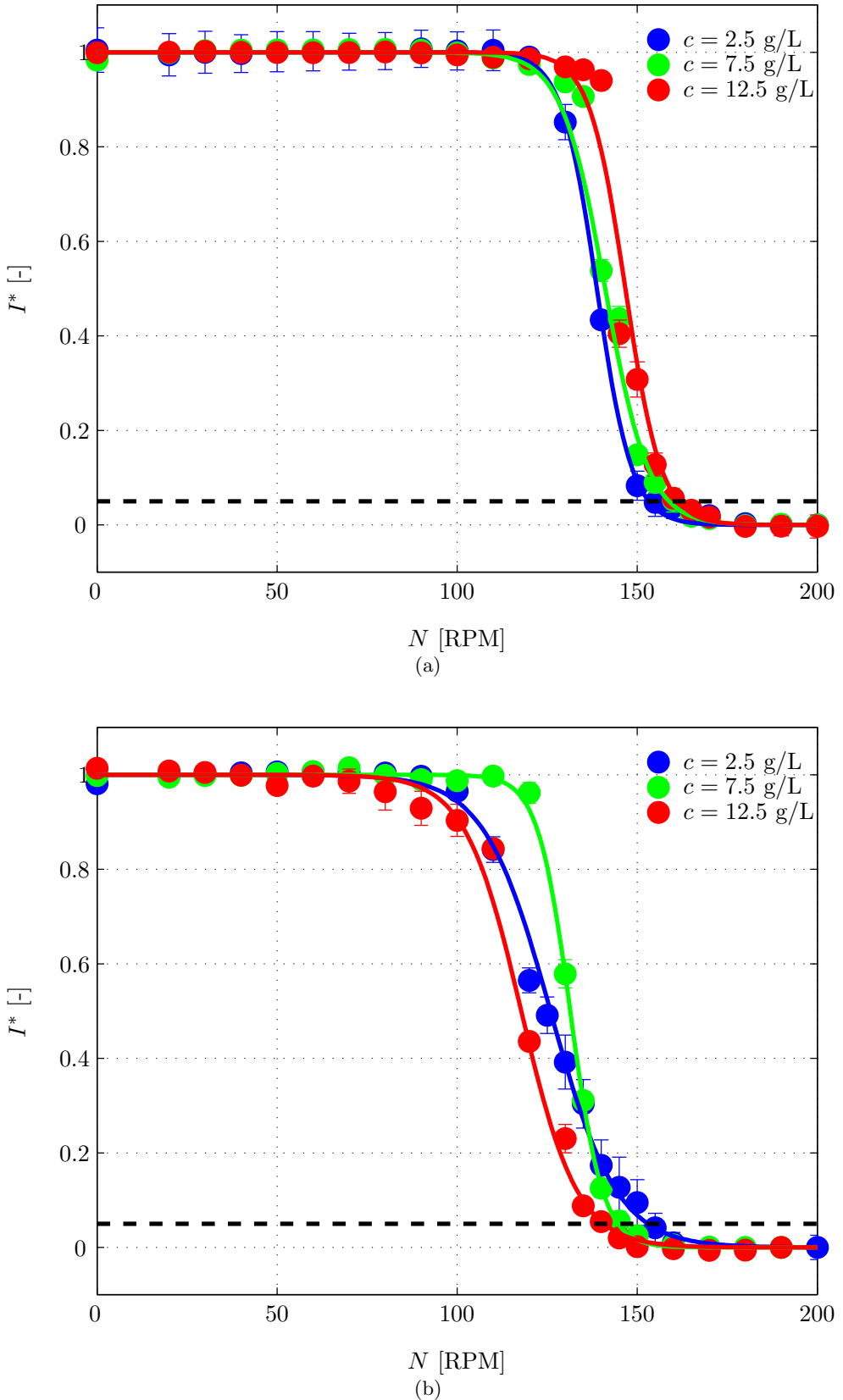


Figure 5: Variation of I^* with shaker speed for different microcarriers' concentrations ($h = 5 \text{ cm}$, $d_i = 7 \text{ cm}$): (a) $d_o = 1.5 \text{ cm}$; (b) $d_o = 2.5 \text{ cm}$.

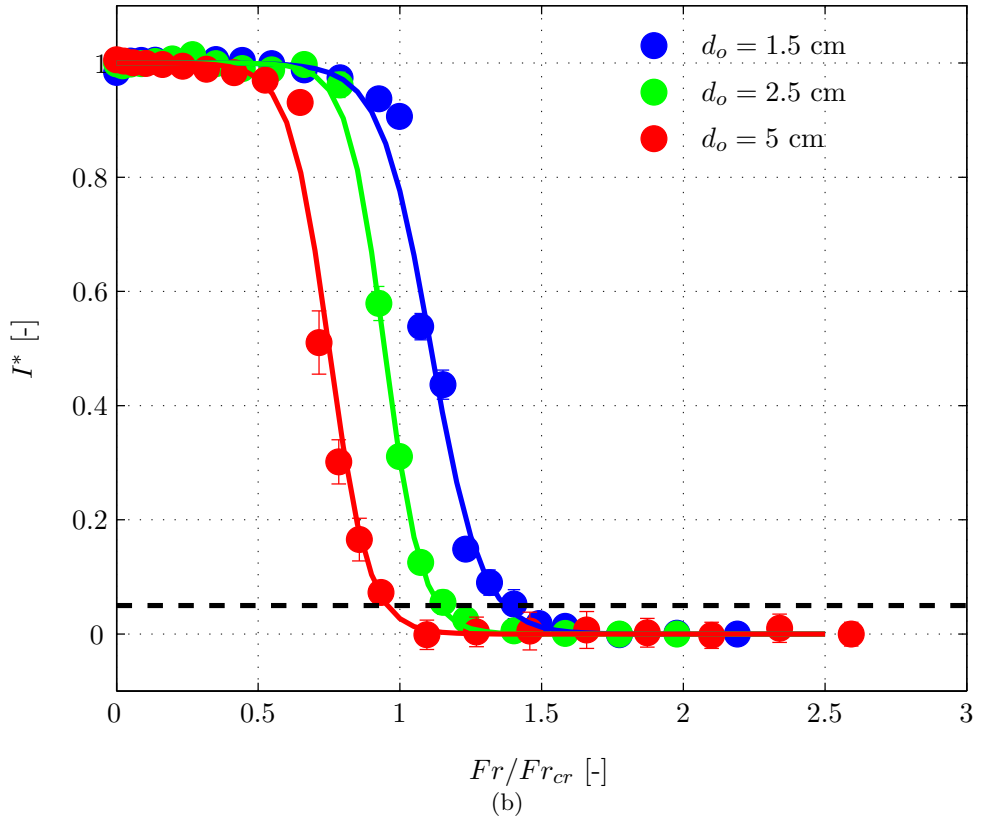
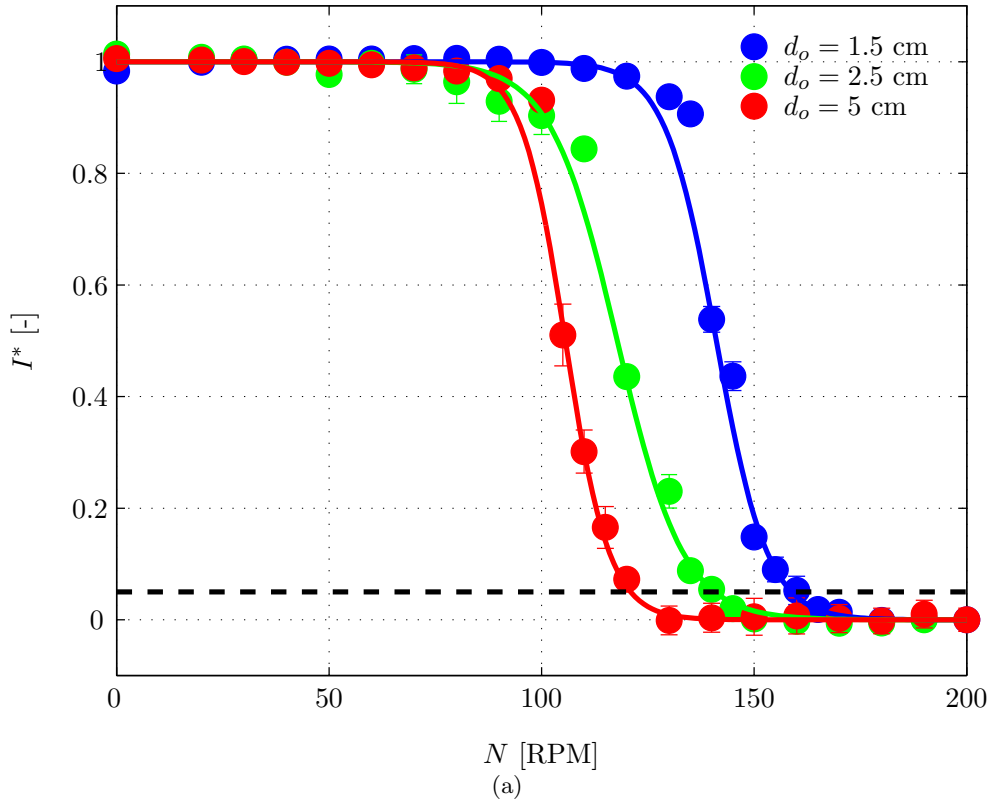


Figure 6: Variation of I^* for different orbital diameters ($h = 5 \text{ cm}$, $d_i = 7 \text{ cm}$, $c = 2.5 \text{ g/L}$): (a) variation with shaker speed, N ; (b) variation with Fr/Fr_{cr} .

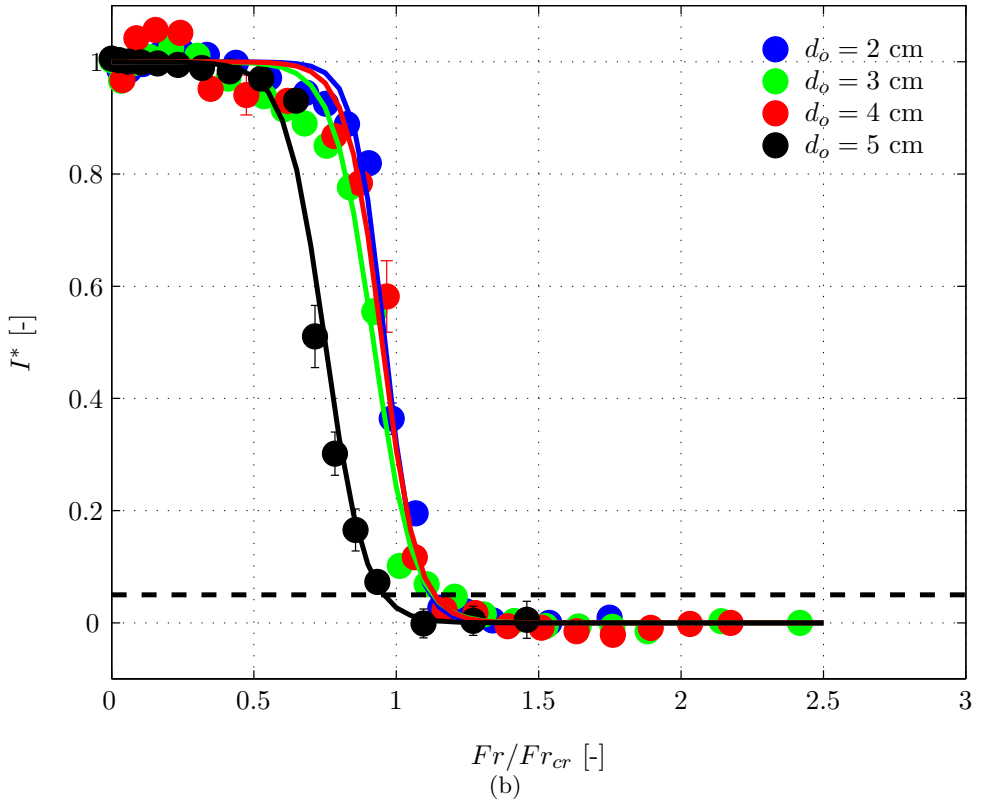
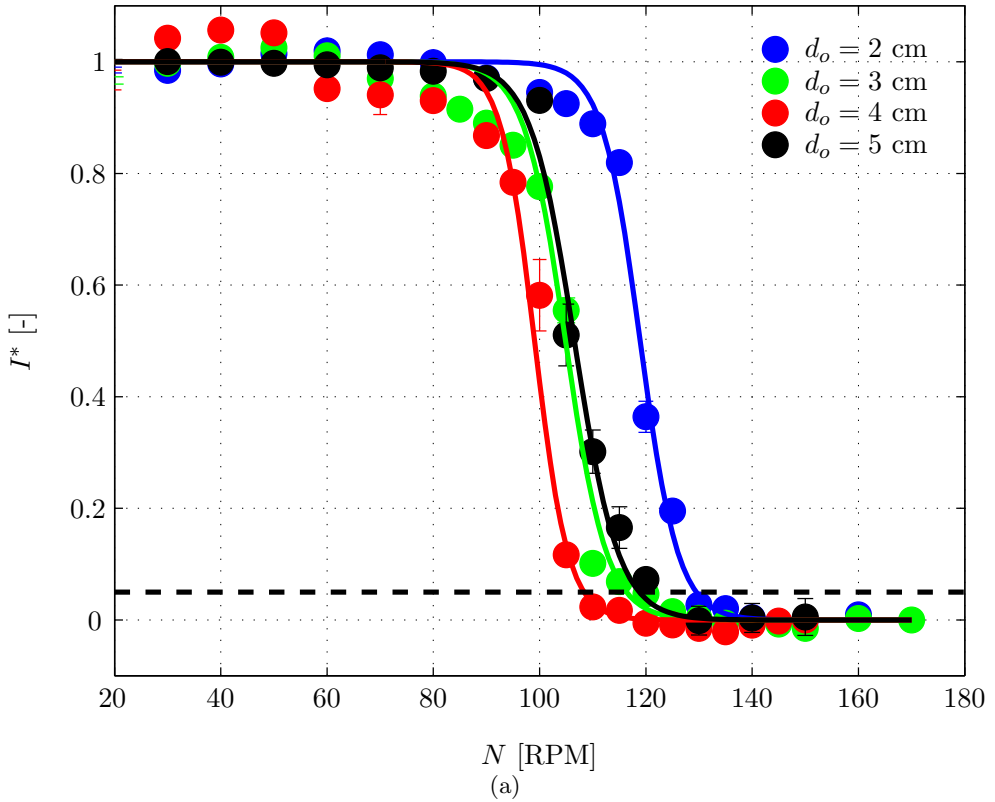


Figure 7: Variation of I^* for different orbital diameters ($h = 3$ and 5 cm, $d_i = 7$ cm, $c = 2.5$ g/L): (a) variation with shaker speed, N ; (b) variation with Fr/Fr_{cr} .

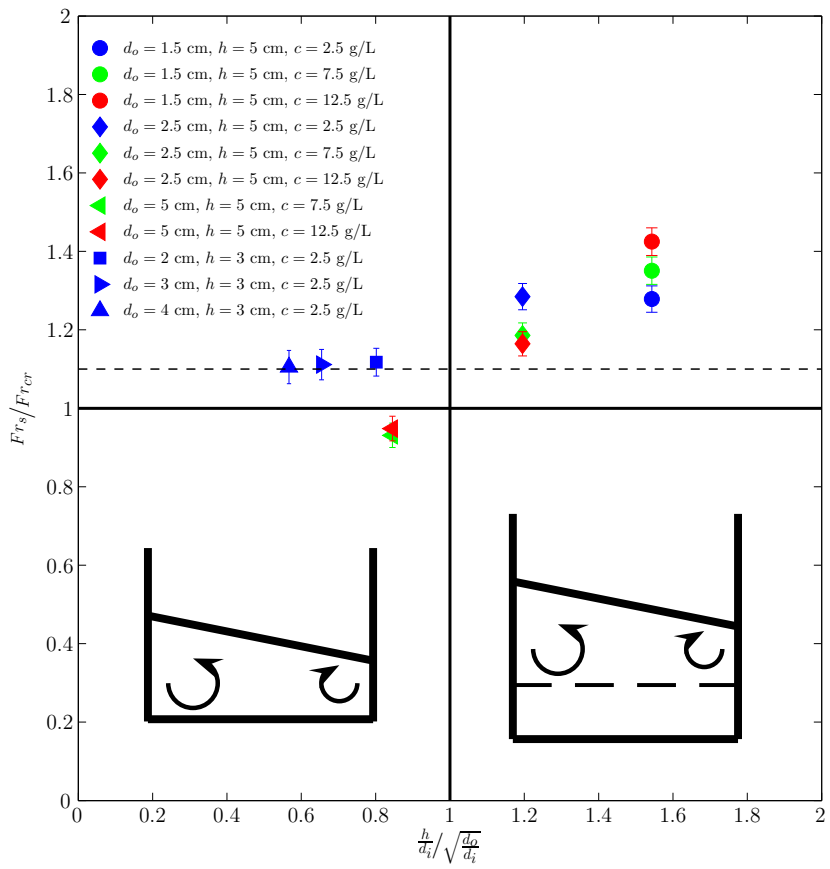


Figure 8: Variation of the suspended to critical Froude number ratio, Fr_s/Fr_{cr} , with critical height ratio, $\frac{h}{d_i}/\sqrt{\frac{d_o}{d_i}}$, for all the conditions investigated.

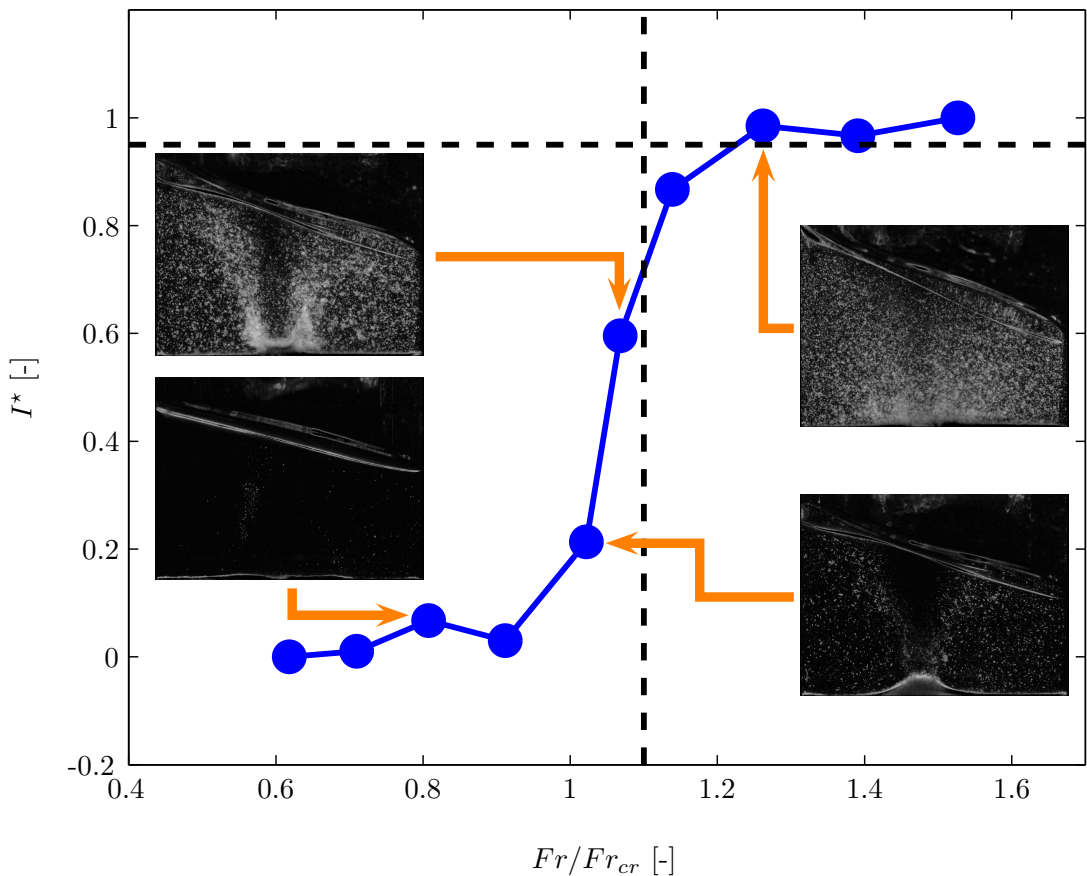


Figure 9: Variation of the normalised brightness index, I^* , with the Froude number ratio, Fr/Fr_{cr} , obtained from measurements on a vertical plane ($d_i = 13$ cm, $d_o = 5$ cm, $h = 6.5$ cm).

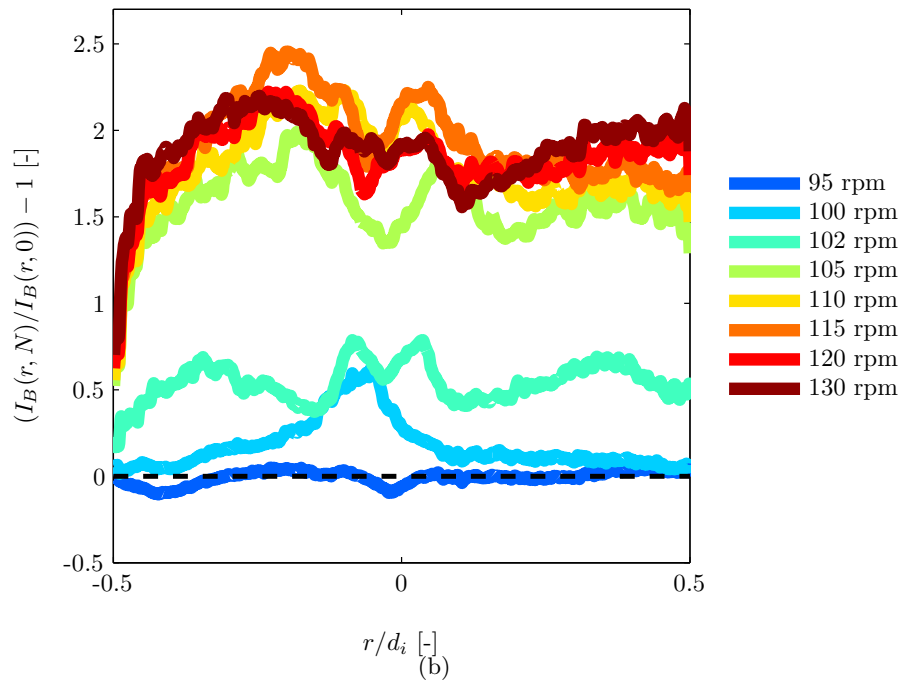
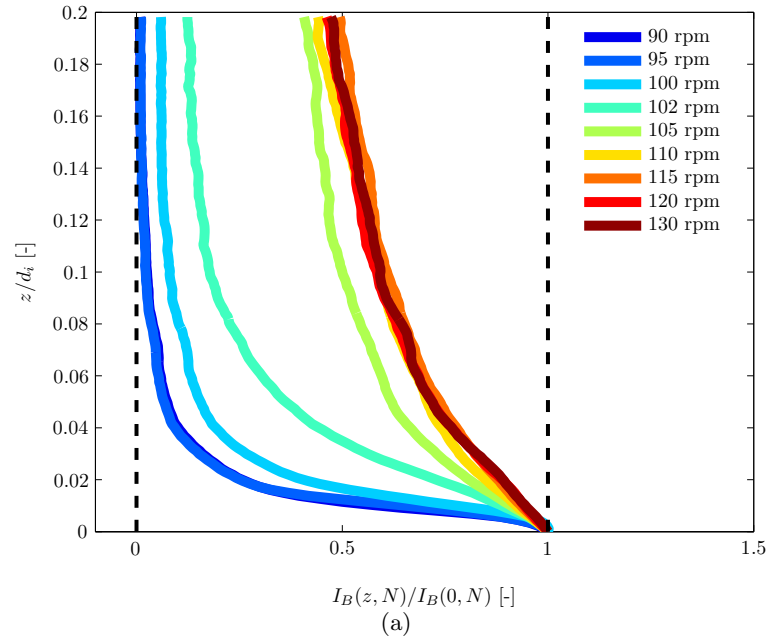


Figure 10: Profiles of the axial and radial cumulative brightness indices for increasing shaken speed ($d_i = 10$ cm, $d_o = 5$ cm, $h = 5$ cm): (a) Axial profiles; (b) Radial profiles.

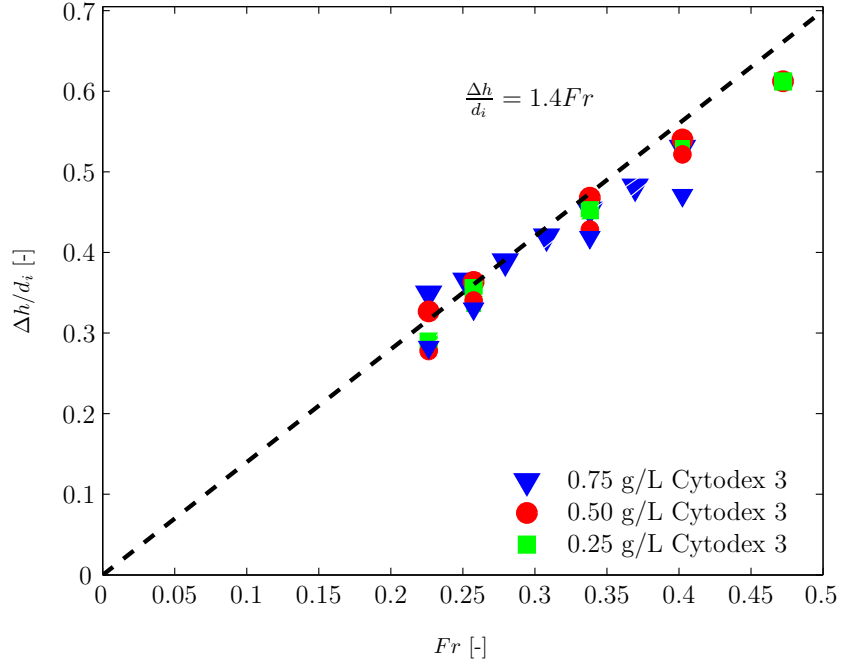


Figure 11: (a) Variation of the non-dimensional wave amplitude, $\Delta h/d_i$, with Froude number, Fr , for different microcarriers' concentrations ($h = 5$ cm, $d_i = 10$ cm, $d_o = 5$ cm).

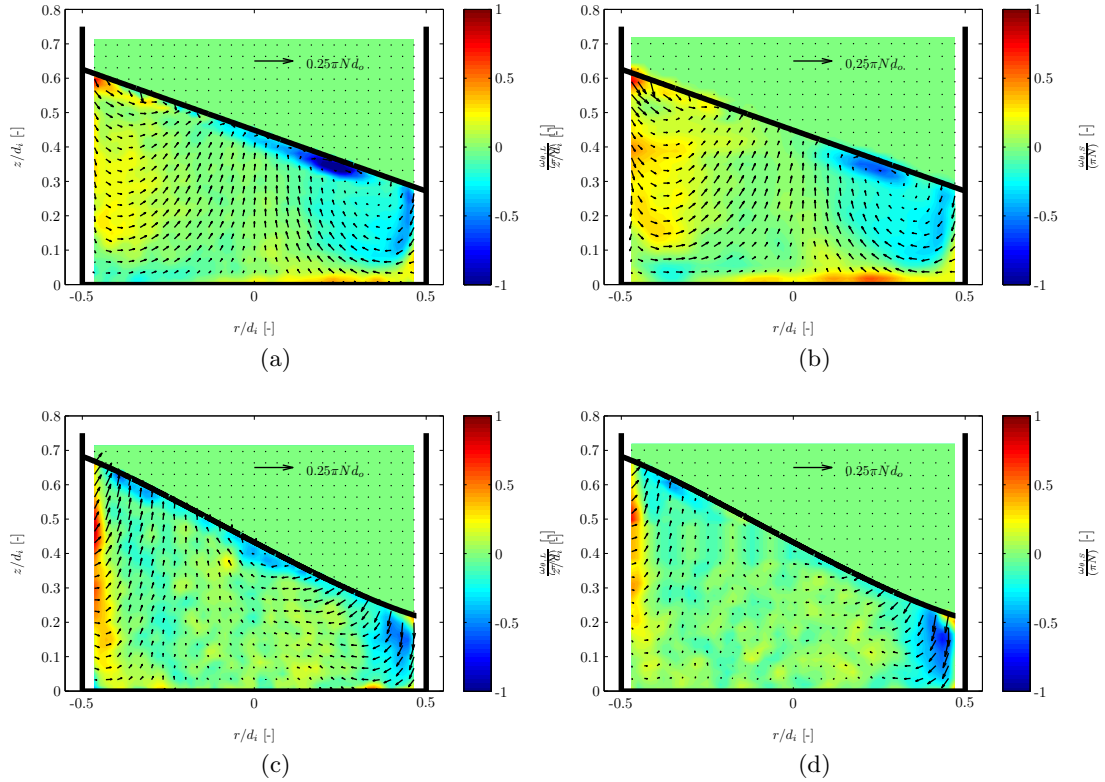


Figure 12: (a) Velocity vector fields and tangential vorticity contour maps of the liquid and solid phases before and after flow transition ($h = 5$ cm, $d_i = 10$ cm, $d_o = 5$ cm, $c = 0.5$ g/L): (a) Liquid phase, $N = 90$ RPM; (b) Solid phase, $N = 90$ RPM; (c) Liquid phase, $N = 110$ RPM; (d) Solid phase, $N = 110$ RPM .